



In-situ exsolved NiS nanoparticle-socketed CdS with strongly coupled interfaces as a superior visible-light-driven photocatalyst for hydrogen evolution

Kailu Li, Hui Pan, Fang Wang, Zhengguo Zhang, Shixiong Min^{*}

School of Chemistry and Chemical Engineering, North Minzu University, Yinchuan 750021, PR China

ARTICLE INFO

Keywords:

CdS particles
NiS cocatalyst
In-situ exsolution
Visible light
H₂ evolution

ABSTRACT

Herein, a NiS nanoparticle-socketed CdS photocatalyst (NiS/CdS-*e*) is developed by hydrothermal sulfurization of Ni-doped Cd(OH)₂ precursor, where the Cd(OH)₂ particles are converted into CdS while the doped Ni species are exsolved and socketed on the surfaces of CdS. 2% NiS/CdS-*e* presents a high H₂ evolution rate of 18.9 mmol g⁻¹ h⁻¹ with an apparent quantum efficiency (AQE) of 13.9% at 420 nm, much superior to those of pristine CdS (0.5 mmol g⁻¹ h⁻¹) and 2% NiS/CdS-*h* (9.9 mmol g⁻¹ h⁻¹) prepared by impregnation-hydrothermal sulfurization. The enhanced activity originates from the strongly coupled interface between exsolved NiS and CdS that efficiently promote the charge separation, while the exsolved NiS nanoparticles serve as highly active H₂ evolution sites. Moreover, the strongly coupled interfaces enable improved H₂ evolution stability for 2% NiS/CdS-*e* over a 30-h cycling reaction. This work provides an effective strategy toward strongly coupled cocatalyst/semiconductor photocatalysts for efficient solar energy conversion.

1. Introduction

H₂ energy is considered as a good alternative energy to solve the current energy crisis because of its high energy density and its combustion product is only water without carbon emission. Photocatalytic water splitting using solar light and semiconductor-based photocatalysts has been considered as one of the most promising solutions toward the sustainable production of H₂ [1–4]. Although many semiconductor-based photocatalysts have been found to be capable of photocatalytically splitting H₂O to produce H₂, the overall solar-to-H₂ energy conversion efficiency is still low and far from practical application. Over past three decades, extensive efforts have been devoted to design and construct efficient semiconductor-based photocatalysts [5–7]. Among various approaches, loading suitable and efficient cocatalysts on the surfaces of semiconductor particles has been proven to be one of the most effective strategies to enhance the photocatalytic performance of resulting heterogeneous photocatalysts [8,9]. In general, cocatalysts could not only greatly promote the charge separation and transfer driven by junctions/interfaces formed between cocatalyst and semiconductor but also serve as the active sites for efficiently catalyzing the surface redox reactions [10,11].

Recently, the efficiency and the price-performance ratio of

photocatalytic H₂ evolution reaction on semiconductor photocatalysts have been greatly improved upon the use of non-expensive cocatalysts based on earth-abundant elements (Fe, Co, Ni, Cu, Mo, W, etc.) [12–15]. Among the developed photocatalysts so far, transition metal sulfides (MoS_x, CoS, NiS_x, and WS_x) as cocatalysts loaded on visible-light-responsive CdS have been frequently studied for various photocatalytic applications such as water splitting and CO₂ reduction due to the maximum solar light utilization efficiency and high performance [16–23]. However, these cocatalysts are traditionally loaded on the surface of semiconductor photocatalysts by means of impregnation [24,25], photodeposition [26,27], and hydrothermal reactions [28,29]. Some of these methods are easy to access but typically fail to establish a strongly coupled interface between cocatalyst and semiconductor, which is unfavorable for the electron transfer from semiconductor to loaded cocatalyst, thus limiting the charge separation efficiency [30]. On the other hand, above methods are also ineffective to control the dispersion, size, and valence states of the loaded cocatalysts, which would further reduce the number of achievable active sites and thus diminish the H₂ evolution activity and stability of resulting cocatalyst/semiconductor photocatalysts. Therefore, effective loading methods are still highly desirable to access highly active cocatalyst-loaded semiconductor photocatalysts with a strongly coupled

^{*} Corresponding author.

E-mail address: sxmin@nwnu.edu.cn (S. Min).

<https://doi.org/10.1016/j.apcatb.2022.122028>

Received 2 August 2022; Received in revised form 25 September 2022; Accepted 27 September 2022

Available online 29 September 2022

0926-3373/© 2022 Elsevier B.V. All rights reserved.

interface for achieving high-performance photocatalytic water splitting for H_2 production.

Recently, the in-situ lattice exsolution strategy, based on the doped metal species in-situ exsolved from the parents such as perovskite oxides under reductive conditions [31,32], has been developed as an effective approach to prepare loaded catalysts on various parent substrates for catalysis applications such as solid oxide fuel cells [33,34], high-temperature steam electrolysis [35,36], electrocatalytic H_2 and O_2 evolution reactions [37], methane/ethanol reforming [38,39], and so on. Attributing to the enhanced dispersion of loaded catalysts and the strong catalyst-substrate interaction, the exsolved catalysts typically showed enhanced activity and durability in above catalysis reactions. Furthermore, this effective method has also been utilized to exsolve cocatalyst particles on semiconductor photocatalysts for improving the activity of photocatalytic H_2 evolution. For instance, the in-situ exsolved WS_x nanodots on $SrTiO_3$ via H_2 reduction followed by sulfurization have shown enhanced catalytic activity compared to the directly loaded WS_x [40]. In addition, the in-situ exsolution of Ag nanoparticles on single $AgTaO_3$ and its composite with $SrTiO_3$ ($AgTaO_3$ - $SrTiO_3$) by chemical reduction can also greatly improve the activity and stability towards photocatalytic H_2 evolution [41]. However, these exsolution-derived composite photocatalysts are only responsive for the UV light, which limits their capability in harvesting majority of visible light in solar spectrum for large-scale H_2 evolution. Moreover, there is no report on employing this exsolution strategy to prepare visible-light-responsive metal sulfide photocatalysts towards photocatalytic H_2 evolution with high performance.

In this work, we propose an effective in situ exsolution strategy to fabricate a strongly coupled NiS nanoparticle-socketed CdS photocatalyst (NiS/CdS-e) for high-performance photocatalytic H_2 evolution under visible light via the one-step hydrothermal sulfurization of Ni-doped $Cd(OH)_2$ precursor. During sulfurization, the conversion of $Cd(OH)_2$ to CdS nanoparticles and the simultaneous exsolution of doped Ni species into NiS nanoparticles can be accomplished in one step reaction, avoiding the following post deposition of NiS and further post-treatment, which greatly simplifies the preparation and performance optimization of NiS/CdS-based photocatalysts for large-scale application. By taking the advantages of developed in situ exsolution method, a strongly coupled interface and large contact area between NiS and CdS are achieved in as-prepared NiS/CdS-e photocatalysts to efficiently address the sluggish charge transfer and low charge separation efficiency, two long-standing issues requiring the development of effective photocatalyst preparation method. We also demonstrate that the exsolution-derived NiS/CdS-e exhibits remarkably high activity and stability towards photocatalytic H_2 evolution under visible light irradiation, which is much superior to those of surface NiS nanoparticle-deposited CdS (NiS/CdS-h) prepared by traditional impregnation-hydrothermal sulfurization method. Spectroscopic, electrochemical and photoelectrochemical characterizations reveal the crucial role of strongly coupled interface in enhancing charge separation efficiency by promoting charge transfer and the formation of exsolved NiS nanoparticles as highly active sites in catalyzing H_2 evolution reaction with a lower overpotential.

2. Experimental section

2.1. Chemicals and materials

All chemicals were of analytical grade and used as received without further purification. $Cd(NO_3)_2 \cdot 4H_2O$ was purchased from Tianjin Huadong Reagent Factory, $Ni(NO_3)_2 \cdot 6H_2O$ was purchased from Shanghai Zhongqin Chemical Reagent Co., Ltd., NaOH ($\geq 98\%$) was purchased from Shanghai TITAN Technology Co., Ltd., Thioacetamide ($\geq 99\%$) was purchased from Aladdin Reagent. All solutions used throughout the experiments were prepared with ultrapure water (18.2 M Ω cm).

2.2. Preparation of photocatalysts

2.2.1. Preparation of Ni-doped $Cd(OH)_2$ and pristine $Cd(OH)_2$ precursors

The Ni-doped $Cd(OH)_2$ (Ni/Cd($OH)_2$) precursors were first prepared according to the reported method with minor modifications [42]. In brief, 0.01 mol of $Cd(NO_3)_2 \cdot 4H_2O$ and a certain amount of Ni ($NO_3)_2 \cdot 6H_2O$ were dissolved in 20 mL of H_2O under stirring, to which a 20 mL of NaOH solution (1.6 M) was slowly added. After being stirred for 30 min, the obtained precipitates were collected by filtration and washed with H_2O for three times. Then, the wet precipitates were redispersed into 30 mL of H_2O with ultrasonication to obtain a homogenous suspension. Afterwards, the suspension was transferred into a Teflon-lined autoclave and heated in an oven at 180 °C for 12 h. The obtained products were collected, washed with H_2O , and dried in a vacuum oven at 60 °C overnight. The obtained products were denoted as x% Ni/Cd($OH)_2$, where the x represents the molar ratio of Ni to Cd.

The pristine $Cd(OH)_2$ precursor was prepared by the identical processes for x% Ni/Cd($OH)_2$ except the addition of $Ni(NO_3)_2 \cdot 6H_2O$.

2.2.2. Preparation of NiS/CdS-e and pristine CdS photocatalysts

The as-prepared x% Ni/Cd($OH)_2$ precursors were reacted with thioacetamide (TAA) as S source under hydrothermal conditions to convert $Cd(OH)_2$ to CdS and simultaneously exsolve the doped Ni into Ni sulfides on the surface of CdS. In a typical procedure, 1 g of x% Ni/Cd($OH)_2$ was first dispersed in 20 mL of H_2O to form a homogenous suspension by ultrasonication. Then 1.875 g of thioacetamide (TAA) was added to the above suspension and stirred for 30 min. The resulting mixture was then transferred into a Teflon-lined autoclave and the sealed autoclave was heated at different temperatures (160–220 °C) for a certain time (10–20 h). The obtained products were collected, washed with H_2O and absolute ethanol, and finally dried in a vacuum oven at 60 °C overnight. The obtained products were denoted as x% NiS/CdS-e.

The pristine CdS was prepared by reacting pristine $Cd(OH)_2$ precursor with TAA using the same procedure for the preparation of x% NiS/CdS-e.

2.2.3. Preparation of NiS/CdS-h photocatalysts

For comparison, NiS physically loaded CdS (x% NiS/CdS-h) photocatalysts were prepared through a hydrothermal deposition method as follows: 1 g of as-prepared pristine CdS (Section 2.2.2) was dispersed into 20 mL of H_2O containing a certain amount of $Ni(NO_3)_2 \cdot 6H_2O$ (Ni/Cd = x%) by ultrasonication followed by adding 1.5 g of TAA. After stirring for 30 min, the resulting mixture was transferred into a Teflon-lined autoclave, which was heated at 180 °C for 12 h. After that, the obtained x% NiS/CdS-h products were collected by vacuum filtration, washed with H_2O and absolute ethanol, and finally dried in a vacuum oven at 60 °C overnight.

2.3. Characterization

X-ray diffraction (XRD) patterns of the samples were recorded with a Rigaku Smartlab diffractometer with a Ni-filtrated $Cu K\alpha$ radiation. X-ray photoelectron spectroscopy (XPS) of the samples was performed on a Thermo Scientific Escalab-250Xi XPS spectrometer using an Al $K\alpha$ X-ray source. Transmission electron microscopy (TEM) and high-resolution TEM (HRTEM) images were taken with JEM F200 and FEI Talos F200X field emission electron microscope. UV–vis diffuse reflectance spectra were recorded on a PerkinElmer Lambda-750 UV–vis–near-IR spectrometer equipped with an integrating sphere, and $BaSO_4$ powders were used as a reflectance standard. The concentrations of elements in reaction solution were determined by using an inductively coupled plasma mass spectrometer (Agilent 7800). The steady-state photoluminescence spectra of the catalysts dispersed in a 10% lactic acid (LA, pH 1.2) solution upon excitation at 370 nm were measured using a Horiba Science Fluoromax-4 fluorescence spectrophotometer. The PL decay spectra were measured using a Horiba Jobin Yvon Data Station

operated in time-correlated single-photon counting (TCSPC) module at 370 nm laser excitation with a time resolution of 200 ps and a repetition rate of 1 MHz. Light-scattering Ludox solution was used to obtain the instrument response function (prompt). The fitting of the decay curves was completed on a Horiba Jobin Yvon DAS6 fluorescence attenuation analysis software.

2.4. Photocatalytic H₂ evolution experiments

The photocatalytic H₂ evolution experiments were carried out in a 250 mL reaction cell equipped with a 300 W Xenon lamp (HSX-F/UV300) with a cutoff filter of 420 nm as the light source. In a typical experiment, 50.0 mg of the photocatalyst was added into the reaction cell containing 100 mL of 10 vol% lactic acids (LA, pH 1.2) aqueous solution as the sacrificial reagent by ultrasonication for 5 min. Prior to light irradiation, the reaction system was thoroughly degassed to remove the oxygen inside the reactor and dissolved in solution. The reaction solution was continuously stirred and maintained at room temperature by a cooling water flow. The amount of H₂ gas produced was determined by a gas chromatograph (CEL-GC-7900, TCD, N₂ carrier).

The photocatalytic H₂ evolution stability of the samples was evaluated by performing a continuous cycling reaction over a period of 30 h in a 100 mL of 10 vol% LA solution with a pH value of 5 (adjusted by adding NaOH). After each 5 h reaction, the reaction system was evaluated and purged with N₂ and then directly reused for next cycle without the separation of photocatalyst. The other reaction conditions for stability test were kept as the same for activity test.

The apparent quantum efficiency (AQE) of H₂ evolution was measured under the visible light irradiation with different wavelengths obtained by using different bandpass filters (420, 475, 520, and 550 nm) and 300 W Xenon lamp. The incident light photon flux was determined using a Ray virtual radiation actinometer (Apogee MQ-500, Silicon Ray detector, spectrum, 389–692 nm; measuring range: 0–4000 mol^{−1} m^{−2} s^{−1}). The AQE is calculated from the ratio of the number of reaction electrons (n_{H_2}) to the number of incident photons (n_p) according to the Eq. (1):

$$AQE(\%) = \frac{2 \times n_{H_2}}{n_p} \times 100\% \quad (1)$$

2.5. Electrochemical and measurements

All the electrochemical and photoelectrochemical measurements were performed in a standard three-electrode system using an electrochemical workstation (Cortest, Wuhan, China). A Pt mesh (1 cm × 1 cm) and a saturated Ag/AgCl electrode were used as the counter and reference electrodes, respectively. The working electrode was fabricated by the drop-coating method. 10 mg photocatalyst powder was first dispersed by ultrasound into a mixture of 1 mL ethanol solution, 2 mL of deionized water and 20 μL of 1 wt% Nafion-ethanol solution. Then, 0.4 mL of the photocatalyst suspension was drop-coated on carbon paper (CP, 1.5 cm × 1.5 cm) and dried at 50 °C for 24 h. The geometric surface area of the working electrode in the electrolyte was controlled to be 2.25 cm². To ensure the stability of the working electrode, a mixed solution of 0.5 M Na₂SO₄ containing 10 vol % LA was used as the supporting electrolyte. A 300 W Xenon lamp equipped with a 420 nm cutoff filter was used as the light source. The linear sweep voltammetry (LSV) measurements were carried out at a scan rate of 10 mV s^{−1}. Electrochemical impedance spectroscopy (EIS) measurements were performed at a bias of 0.5 V vs. Ag/AgCl electrode in the frequency range of 10 MHz to 100 kHz with an AC amplitude of 5 mV. The Mott-Schottky analysis was conducted from −1.2 to 0.2 V at a frequency of 100 kHz with a step of 10 mV and an AC amplitude of 10 mV. The transient photocurrent response was recorded at a bias of 0.5 V vs. Ag/AgCl under chopped visible light irradiation.

3. Results and discussion

3.1. In-situ exsolution strategy toward strongly coupled photocatalysts

The synthesis procedure of NiS/CdS-e via the in-situ exsolution strategy is schematically shown in Fig. 1a. The Ni doped Cd(OH)₂ (Ni/Cd(OH)₂) precursors were first synthesized through the hydrothermal reaction of Cd(NO₃)₂ and Ni(NO₃)₂ under alkaline conditions according to the procedures reported in the literature [42]. The as-obtained Ni/Cd(OH)₂ precursors were characterized using X-ray diffraction (XRD). As indicated in Fig. 1b and Fig. S1, the XRD patterns of Ni/Cd(OH)₂ precursors match well with that of pristine Cd(OH)₂ (JCPDS No. 73–0969). There are no peaks of NiO or Ni(OH)₂ even at higher doping amounts of Ni, suggesting that Ni ions are homogeneously doped into the crystal lattice of Cd(OH)₂. In addition, in comparison with that of pristine Cd(OH)₂, the diffraction peak of Ni/Cd(OH)₂ precursors at 2θ value of around 18.7° is gradually shifted to the higher values with increasing Ni doping amount because of the shrink of the cell volume as a result of the replacement of the larger Cd²⁺ cation (0.97 Å) with the smaller Ni²⁺ cation (0.69 Å) [43]. The Ni/Cd(OH)₂ precursors were then converted to NiS/CdS-e via the low temperature hydrothermal sulfurization process using TAA as the S source, during which the Cd(OH)₂ was transformed into CdS. At the same time, the doped Ni exsolved from the crystal lattice generating NiS on the surface of CdS (Fig. 1a, route I) to obtain NiS/CdS-e photocatalysts with strongly coupled interfaces. As revealed by the XRD analysis, the XRD patterns of NiS/CdS-e photocatalysts are in line with that of the pristine CdS (Fig. 1b and Fig. S2), which is well-crystallized in the hexagonal phase (JCPDS No. 41–1049) [44], indicating the completed conversion of Cd(OH)₂ into CdS during the hydrothermal sulfurization process. Notably, in the XRD patterns of NiS/CdS-e photocatalysts, a new peak at 30.5°, corresponding to the hexagonal NiS (JCPDS No. 12–0041) can be clearly identified (see the TEM analysis below), confirming the efficient exsolution of doped Ni ions from the lattice of CdS. For comparison, the Ni sulfides were also loaded on the surface of CdS by a traditional impregnation-hydrothermal sulfurization method to prepare NiS/CdS-h photocatalysts (Fig. 1a, route II). In contrast to NiS/CdS-e photocatalysts, there are no peaks attributing to any Ni sulfides that could be detected in the XRD patterns of NiS/CdS-h photocatalysts (Fig. 1b and Fig. S3), which may be due to the low crystallinity of loaded Ni sulfides [45]. Moreover, the (101) peak of CdS in NiS/CdS-e is slightly shifted to a higher value while that of NiS/CdS-h keeps unchanged relative to pristine CdS, which also indicates that there is a strongly coupled interaction between the exsolved NiS and CdS substrate.

3.2. Chemical states and structural features of in-situ exsolved cocatalyst

The chemical states of the samples were examined using X-ray photoelectron spectroscopy (XPS). As revealed by the XPS survey spectra in Fig. S4, in addition to Cd and O, a strong Ni peak is found in 2% Ni/Cd(OH)₂ compared to pristine Cd(OH)₂, confirming the successful doping of Ni into the lattice of the Cd(OH)₂. After the hydrothermal sulfurization, an obvious S peak appears in the resulting CdS and 2% NiS/CdS-e, and the content of O element significantly decreases, demonstrating that the OH[−] in the Cd(OH)₂ and 2% Ni/Cd(OH)₂ was replaced by S^{2−}. The high-resolution Ni 2p spectra of 2% Ni/Cd(OH)₂, 2% NiS/CdS-e, and 2% NiS/CdS-h are shown in Fig. 2a. For 2% Ni/Cd(OH)₂, the two peaks at 856.1 and 873.5 eV can be identified as the Ni 2p_{3/2} and Ni 2p_{1/2} peaks of the Ni(OH)₂, respectively, and the intense satellite peaks found at 861.9 and 879.7 eV belong to the Ni²⁺ ions in Ni(OH)₂ [46], which further confirms the Ni²⁺ has been doped into the lattice of Cd(OH)₂. After sulfurization, besides the characteristic peaks ascribed to Ni(OH)₂ (Ni 2p_{3/2}, 856.3 eV; Ni 2p_{1/2}, 874.0 eV), there are two new peaks at 853.7 and 871.3 eV along with their satellite peaks at 859.1 and 876.9 eV in the Ni 2p spectrum of 2% NiS/CdS-e, which can be assigned to a doublet Ni 2p_{3/2} and Ni 2p_{1/2} of Ni-S species [47],

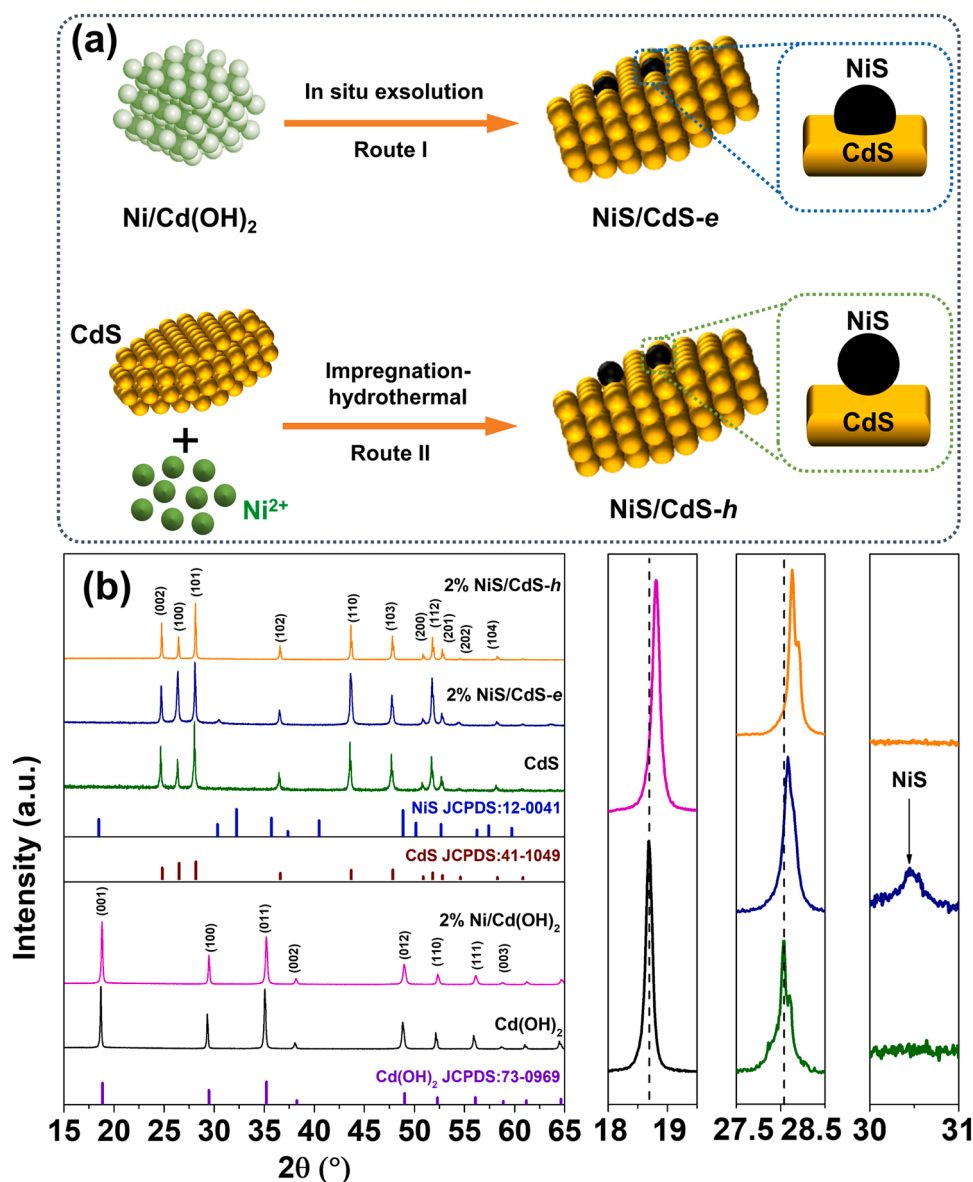


Fig. 1. (a) Schematic illustration of the synthesis process of NiS/CdS-e and NiS/CdS-h photocatalysts. (b) XRD patterns of the pristine Cd(OH)_2 , 2% Ni/Cd(OH)_2 , pristine CdS, 2% NiS/CdS-e, and 2% NiS/CdS-h.

respectively, which suggest that the exsolved Ni species are mainly in the form of NiS on the surface of CdS, consistent with the XRD in Fig. 1b. Similarly, the Ni 2p spectrum of 2% NiS/CdS-h also shows two doublet Ni 2p_{3/2} and Ni 2p_{1/2} peaks at 856.4 and 873.9 eV for Ni(OH)₂ and 853.8 and 871.3 eV for NiS, each followed by the corresponding satellite peaks, which correspond to Ni(OH)₂ and Ni-S bonds, respectively. However, it can be noted that the Ni 2p_{3/2} peak of Ni-S bond in 2% NiS/CdS-e occurs at a slightly lower binding energy (~0.1 eV) relative to those of in 2% NiS/CdS-h, which indicates that the oxidation valence state of Ni in Ni-S species of 2% NiS/CdS-e is lower than that of 2% NiS/CdS-h due to the strong interfacial interaction between exsolved NiS and CdS substrate (Fig. 1b). Fig. 2b and c display the high-resolution Cd 3d and S 2p XPS spectra of pristine CdS, 2% NiS/CdS-e, and 2% NiS/CdS-h, respectively. The doublet Cd 3d peaks in pristine CdS locate at 405.1 and 411.8 eV with a spin-orbit separation of 6.7 eV, which are attributed to the Cd 3d_{5/2} and Cd 3d_{3/2} of Cd²⁺, respectively [48]. The S 2p spectrum of CdS can be resolved into two peaks centered at 161.4 and 162.5 eV, which correspond to the S 2p_{3/2} and S 2p_{1/2} and of S²⁻, respectively [49]. These results confirm the successful conversion of Cd(OH)₂ to CdS during the hydrothermal sulfurization process. The Cd 3d

and S 2p peaks of the 2% NiS/CdS-e occurs at comparable binding energies to those of CdS, which confirms that the conversion of Cd(OH)₂ in 2% Ni/Cd(OH)₂ to CdS. However, the binding energies of Cd 3d and S 2p in the 2% NiS/CdS-e are 0.2 and 0.25 eV lower than those in pristine CdS, respectively, which suggest that a strong interaction is generated between exsolved NiS and CdS attributing to the electron transfer from NiS to CdS. This would create a built-in electric field pointing from NiS and CdS, which would greatly facilitate the transfer of photogenerated electrons from CdS to NiS upon light excitation. In contrast, the Cd 3d and S 2p peaks of 2% NiS/CdS-h are shifted to the higher binding energies compared to those of pristine CdS, indicating that the physical deposition of NiS species on CdS would create a opposite built-in electric field relative to the 2% NiS/CdS-e, which would limit the electron transfer from CdS to loaded NiS, in turn reduce the utilization efficiency of electrons participating in subsequent H₂ evolution reaction. The XPS results confirm the developed in-situ hydrothermal exsolution method is effective to exsolve the NiS on CdS and create a strongly coupled interface between two.

The exsolution of the doped Ni species and the conversion of Cd(OH)₂ into CdS during the hydrothermal sulfurization process were

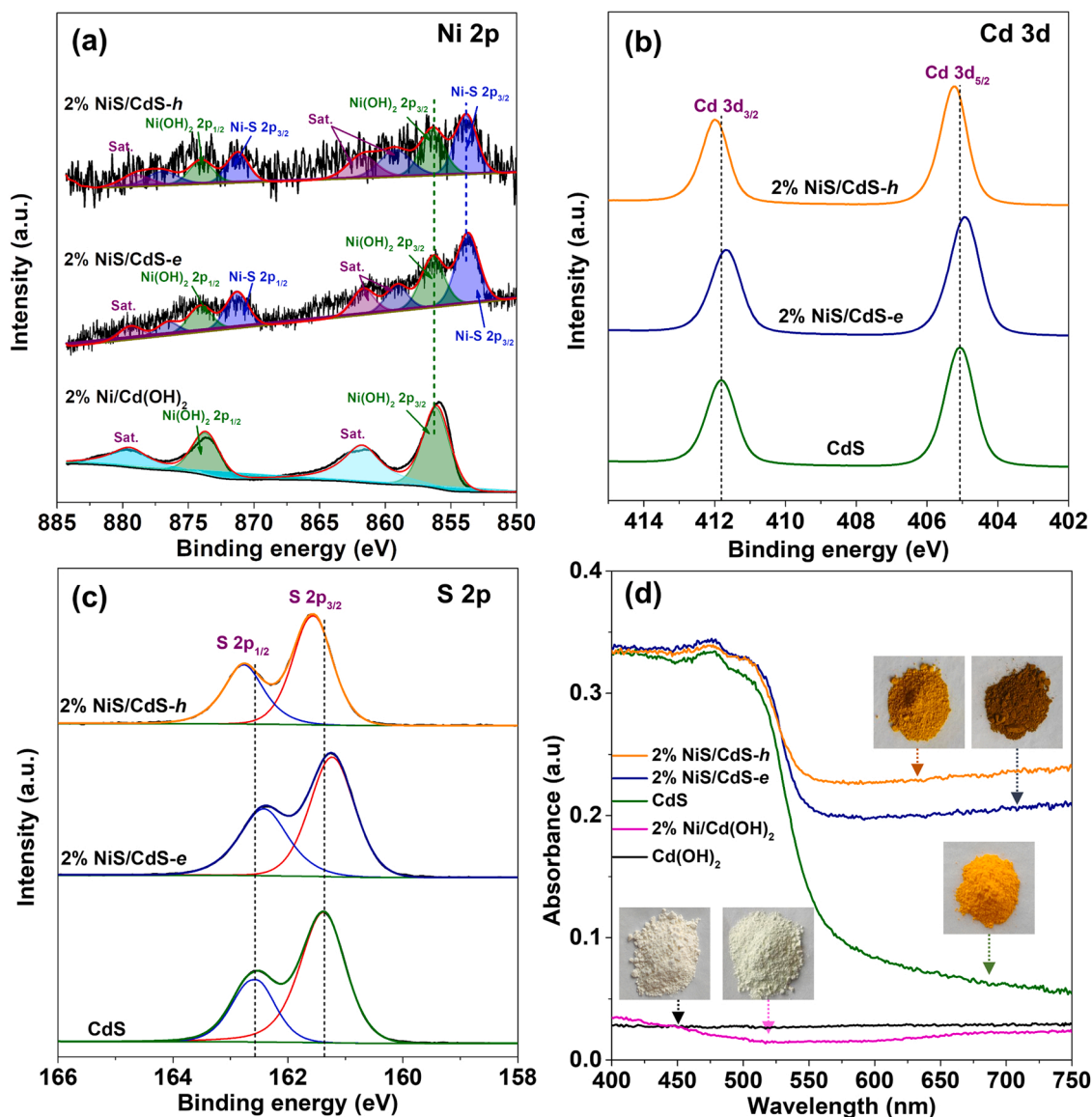


Fig. 2. (a) Ni 2p XPS spectra of 2% Ni/Cd(OH)₂, 2% NiS/CdS-e, and 2% NiS/CdS-h. (b) Cd 3d XPS spectra of pristine CdS, 2% NiS/CdS-e, and 2% NiS/CdS-h. (c) S 2p XPS spectra of pristine CdS, 2% NiS/CdS-e, and 2% NiS/CdS-h. (d) UV-vis diffusion reflectance spectra (UV-vis-DRS) of pristine Cd(OH)₂, 2% Ni/Cd(OH)₂, pristine CdS, 2% NiS/CdS-e and 2% NiS/CdS-h.

further confirmed by UV-Vis diffuse reflectance spectra (UV-Vis DRS). As shown in Fig. 2d, both the Cd(OH)₂ and the 2% Ni/Cd(OH)₂ precursors have no obvious light absorption in the wavelength ranging from 350 to 800 nm, consistent with their white color. In contrast, the pristine CdS resulting from the hydrothermal sulfurization of Cd(OH)₂ precursor shows a typical orange color and exhibits an intense visible light absorption with a threshold of 520 nm, corresponding to a band-gap energy (E_g) of ca. 2.28 eV (Fig. S5), which confirms the effective conversion of Cd(OH)₂ into CdS, consistent with the results of XRD analysis (Fig. 1b). When 2% Ni/Cd(OH)₂ precursor was sulfurized, the absorption threshold of resulting 2% NiS/CdS-e is only slightly red-shifted to 525 nm with a reduced E_g (2.27 eV) compared to pristine CdS, and meanwhile, the absorption in the long-wavelength region (550–800 nm) is significantly improved along with the color change from the orange to brown, which further manifests the exsolution of NiS on the surface of CdS [50]. In addition, with increasing Ni content in Ni/Cd(OH)₂ precursors, the light absorption of the resulting NiS/CdS-e photocatalysts in the long-wavelength region (550–800 nm) gradually increases and the color of the samples changes from orange to dark

brown (Fig. S6) due to the exsolution of more NiS particles on CdS. When NiS was physically loaded on CdS, the light absorption characteristics and E_g (2.27 eV) of NiS/CdS-h samples with different NiS loading are same as that of NiS/CdS-e samples (Fig. S7), but the light absorption of 2% NiS/CdS-h in 550–800 nm region is more intense than that of 2% NiS/CdS-e. This suggests that the NiS particles in NiS/CdS-h sample most likely exist on the surfaces of CdS while the exsolved NiS particles are mainly socketed on the surface of CdS particles with the formation of strongly coupled interfaces.

The evolution of the microstructures and the morphology of the as-prepared 2% NiS/CdS-e photocatalyst were characterized by transmission electron microscope (TEM). As shown in Fig. 3a, the as-synthesized Cd(OH)₂ precursor has a hexagonal sheet-like morphology, which are largely retained after hydrothermal sulfurization (Fig. 3b). The lattice spacing in the corresponding high-resolution TEM image is measured to be 0.324 nm (Fig. 3c), ascribing to the (101) plane of hexagonal CdS, which further confirms the successful conversion of Cd(OH)₂ into CdS. Similar to the Cd(OH)₂ precursor, it is worth noting that the 2% Ni/Cd(OH)₂ still retains the sheet morphology

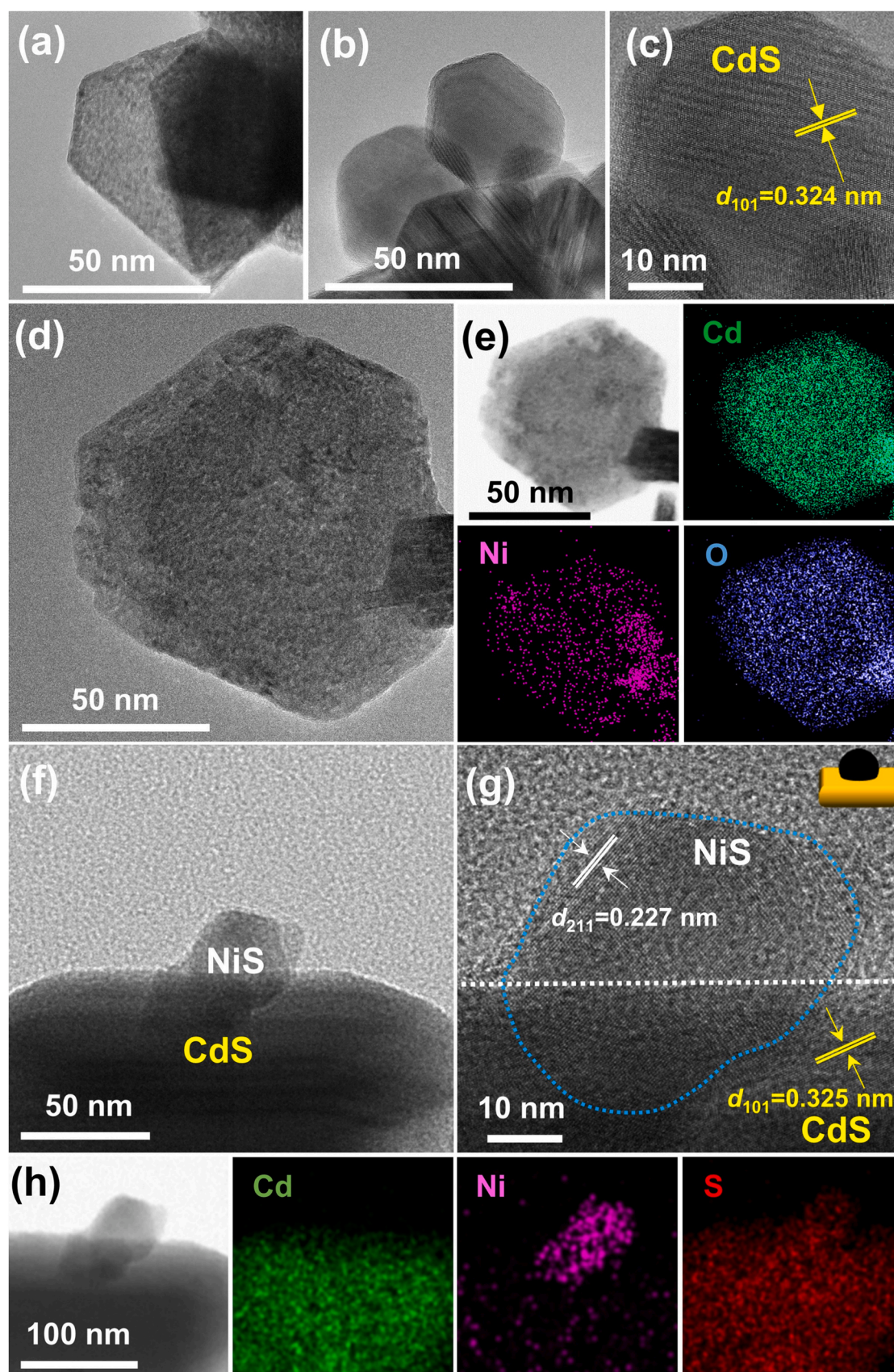


Fig. 3. TEM image of (a) pristine Cd(OH)₂ precursor. (b) TEM and (c) HRTEM images of pristine CdS. (d) TEM and HAADF-STEM images of 2% Ni/Cd(OH)₂ and (e) the corresponding EDX elemental mapping images. (f) TEM, (g) HRTEM, and HAADF-STEM images of 2% NiS/CdS-e and (h) the corresponding EDX elemental mapping images.

of pristine $\text{Cd}(\text{OH})_2$ (Fig. 3d) and no any aggregated particles appear, suggesting the homogenous Ni doping. The high-angle annular dark field scanning transmission electron microscopy (HAADF-SEM) image and the corresponding energy dispersive X-ray spectroscopy (EDX) elemental mapping (Fig. 3e) reveal a uniform distribution of Cd, O, and Ni in 2% Ni/Cd(OH)₂, again confirming the homogenous doping of Ni into lattice of $\text{Cd}(\text{OH})_2$.

Upon the hydrothermal sulfurization of 2% Ni/Cd(OH)₂, the TEM image (Fig. 3f) of the resulting 2% NiS/CdS-e clearly shows that a exsolved particle with a size of ~50 nm is found to be socketed on the surface of CdS. In the corresponding HRTEM image of Fig. 3g, the lattice spacing measured on exsolved particle is 0.227 nm, which agrees well with the (211) plane in NiS, while the lattice spacing determined on substrate is 0.325 nm, corresponding to the (101) plane of CdS [51]. Furthermore, the HAADF-STEM image and the corresponding EDX studies also confirm the exsolution of Ni dopant from the lattice of Cd(OH)₂ during the hydrothermal sulfurization process. As shown in Fig. 3h, unlike the 2% Ni/Cd(OH)₂ where the doped Ni is homogeneously distributed throughout Cd(OH)₂, the Ni distribution in 2% NiS/CdS-e mainly occurs on the exsolved NiS particle while both the Cd and S elements present a uniform distribution on entire sample, which clearly confirms the doped Ni can be effectively exsolved to be NiS particles that are simultaneously socketed on in-situ formed CdS, leading to the formation of strongly coupled interfaces to enable the efficient electron transfer. In strong contrast, the physically loaded NiS particles in 2% NiS/CdS-h severely aggregate on the surface of CdS nanoparticles with a size much larger than those of 2% NiS/CdS-e (Fig. S8), attributed to the weak interaction between loaded NiS and CdS nanoparticles.

3.3. Enhanced photocatalytic H₂ performances of in-situ exsolved photocatalysts

Photocatalytic activities of the samples towards H₂ evolution were evaluated in 10 vol% lactic acid (LA) aqueous solution under visible light irradiation (300 W Xe lamp, $\lambda \geq 420$ nm). The NiS/CdS-e samples prepared at different hydrothermal temperatures and times were first examined for H₂ evolution and it was found that the NiS/CdS-e sample prepared at 180 °C and 12 h exhibits the most favorable H₂ evolution activity (Fig. S9). In the following discussion, the results from the samples prepared under this optimal condition were employed unless noted otherwise. Fig. 4a compares the H₂ evolution activities of CdS, x% NiS/CdS-e, and x% NiS/CdS-h. The pristine CdS shows a very low H₂ evolution activity, and the rate of H₂ evolution is only 0.51 mmol g⁻¹ h⁻¹, attributed to the rapid recombination of photogenerated carriers and holes. In contrast, the x% NiS/CdS-e photocatalysts show significantly enhanced photocatalytic H₂ evolution activity, and the rate of H₂ evolution increases with increasing Ni content and achieves a highest value of 18.9 mmol g⁻¹ h⁻¹ on 2% NiS/CdS-e, which is 37 times faster than that of pristine CdS. The H₂ evolution rate of 2% NiS/CdS-e is also comparable to and even higher than those of recently developed CdS-based photocatalyst loaded with high content transition metal sulfides (>2 wt%) as cocatalysts under visible light (Table S1). This indicates that the exsolved NiS on CdS can serve as an efficient cocatalyst for promoting the H₂ evolution [52,53]. For comparison, the activities of the x% NiS/CdS-h samples were also tested and the results show the activity of CdS can also be greatly enhanced after physically loading NiS cocatalyst compared to CdS, and the activity gradually increases with increasing NiS loading. However, the activities of the x% NiS/CdS-h are

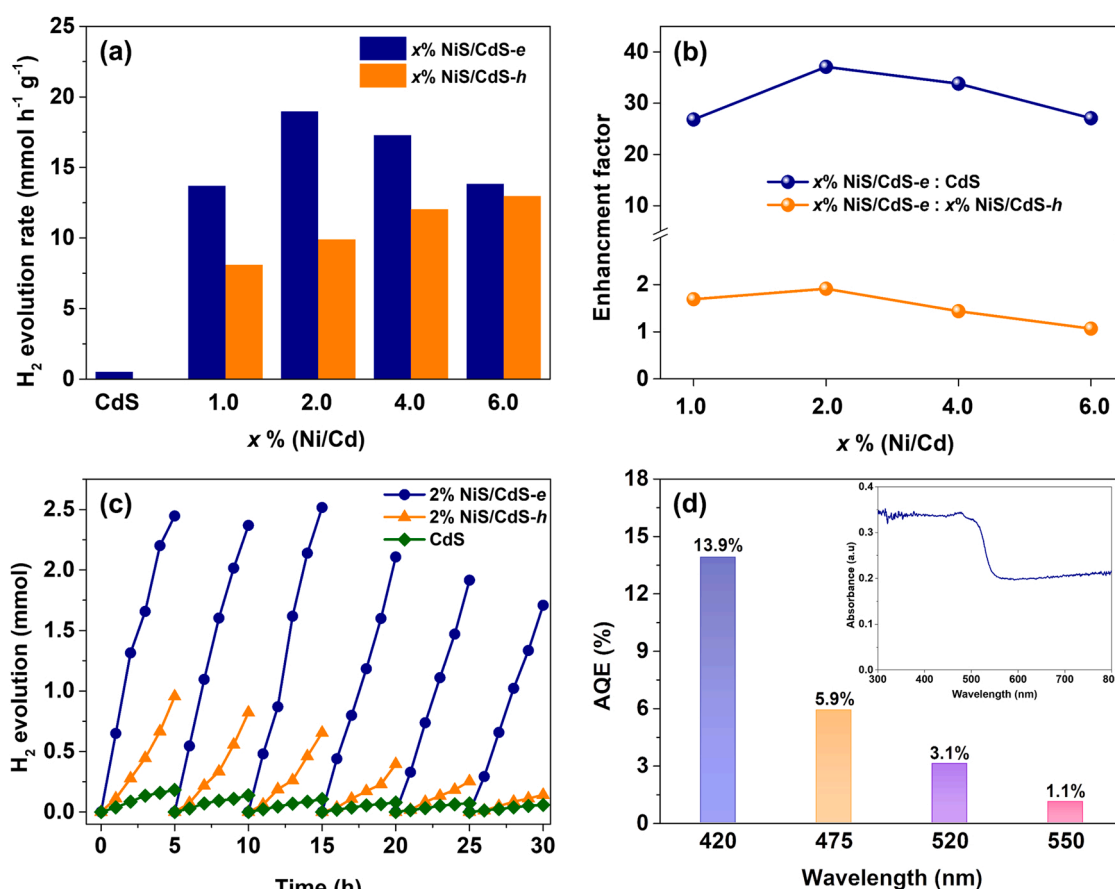


Fig. 4. (a) The rates of photocatalytic H₂ evolution on CdS, x% NiS/CdS-e, and NiS/CdS-h samples. (b) Enhancement factor of H₂ evolution rate by comparing x% NiS/CdS-e with pristine CdS and x% NiS/CdS-h. (c) Photocatalytic H₂ evolution stabilities of pristine CdS, 2% NiS/CdS-h, and 2% NiS/CdS-e. (d) AQE of photocatalytic H₂ evolution on 2% NiS/CdS-e under light irradiation with different wavelengths.

much lower than those of the $x\%$ NiS/CdS-*e* especially at lower Ni contents. As shown in Fig. 4b, the maximum enhancement factor is found to be 2 by comparing the H_2 evolution rate of 2% NiS/CdS-*e* with that of 2% NiS/CdS-*h* ($9.91 \text{ mmol g}^{-1} \text{ h}^{-1}$). This clearly demonstrates that the exsolved NiS are more effective than physically loaded NiS in catalyzing the photocatalytic H_2 evolution reaction on CdS. In addition, we also annealed the 2% NiS/CdS-*h* in a 5% H_2S atmosphere at 300°C for 2 h aiming to strengthen the interfacial interaction between NiS and CdS for enhancing the photocatalytic H_2 evolution activity. As shown in Fig. S10, although the phase structure of annealed 2% NiS/CdS-*h* and the chemical states of NiS keep unchanged, it exhibits a much inferior H_2 evolution activity to unannealed 2% NiS/CdS-*h*. This result further highlights the effectiveness of developed in situ exsolution strategy in this work for preparing strongly coupled photocatalysts with enhanced photocatalytic performance with no need of further post-treatment. It should also be worthy to note that the enhancement factor of H_2 evolution rate of $x\%$ NiS/CdS-*e* comparing $x\%$ NiS/CdS-*h* becomes smaller as the x increases. As indicated in Fig. S11, compared to the 2% NiS/CdS-*e* (Fig. 3f and g), the exsolved NiS particles tend to form large aggregates on CdS at higher Ni contents (4% NiS/CdS-*e* and 6% NiS/CdS-*e*) like the physically loaded NiS does, which would inevitably lead to the reduction of number of active sites achievable and in turn decrease the photocatalytic H_2 evolution activity, as a result, the superiority of the in situ exsolved NiS as a cocatalyst for catalyzing photocatalytic HER would be traded off.

The photocatalytic H_2 evolution stabilities of pristine CdS, 2% NiS/CdS-*h* and 2% NiS/CdS-*e* photocatalysts were tested and the results are given in Fig. 4c. The pristine CdS shows very low stability because of the severe photocorrosion, consistent with the observations in the literature [10]. Although the H_2 evolution activity of 2% NiS/CdS-*h* is enhanced compared to pristine CdS for each cycle, but the activity decreases quickly during the cycling reaction process and only 15% of its initial activity is retained after sixth cycle, which would be mainly due to the detachment of physically loaded NiS from the surfaces of CdS particles since there is no strong connection between loaded NiS and CdS. However, the 2% NiS/CdS-*e* still maintains a higher good H_2 evolution activity (70% retention of its initial activity) even after sixth cycle reaction. The high stability of 2% NiS/CdS-*e* can be attributed to the formation of strongly coupled interfaces between exsolved NiS and CdS, which ensures the strong anchoring and thus high stability of NiS during the long-time reaction process. As revealed by TEM, XRD, and XPS analyses, the NiS particles are still firmly anchored on the surfaces of CdS without the changes in phase structure and chemical states (Fig. S12). Furthermore, we also performed the inductively coupled plasma mass spectroscopy (ICP-MS) experiments to analyze the concentrations of Cd, Ni, and S elements in the reaction solution after a 30-h cycling stability test. As shown in Fig. S13, the concentrations of Cd, Ni, and S elements from the 2% NiS/CdS-*e* reaction solution are significantly lower than those found from the 2% NiS/CdS-*h* reaction solution, suggesting that both the CdS and the NiS in 2% NiS/CdS-*e* are more stable than those in 2% NiS/CdS-*h* due to the formation of strongly coupled interfaces that are effective to prevent the leaching of NiS from the CdS surface and reduce the photocorrosion of CdS.

To further demonstrate the high activity of 2% NiS/CdS-*e*, the apparent quantum efficiency (AQE) of H_2 evolution was measured under the visible light irradiation with different wavelengths. As shown in Fig. 4d, a maximum AQE of 13.9% can be achieved on 2% NiS/CdS-*e* at 420 nm, which is comparable to and even higher than those of recently reported CdS-based photocatalysts loaded with transition metal sulfides as cocatalyst at similar content (Table S1). Note that the change trend of AQE for H_2 evolution on 2% NiS/CdS-*e* somehow derives from its corresponding electronic spectrum (see inset in Fig. 4d). Specifically, although the 2% NiS/CdS-*e* can effectively capture the long-wavelength light (550–800 nm), it shows no H_2 evolution activity at this region. This reveals that the H_2 evolution reaction driven by 2% NiS/CdS-*e* is dominated by the optical absorption property of CdS and the

additionally harvested light originated from the exsolved NiS has no contribution to produce effective photogenerated carries for inducing H_2 evolution reaction on CdS. This also indicates that the exsolved NiS particles on CdS are mainly server as H_2 evolution cocatalyst rather than a light harvester in 2% NiS/CdS-*e* [54].

3.4. Origins of enhanced photocatalytic H_2 evolution performance

To investigate the effect of NiS loading on the charge carrier separation of NiS/CdS photocatalysts, the steady-state photoluminescence (PL) spectra of NiS/CdS photocatalysts were first recorded upon excitation at 370 nm. As shown in Fig. 5a and b, in comparison with pristine CdS that exhibits a strong emission band due to the serve charge recombination [55], the PL emissions for both the NiS/CdS-*e* and NiS/CdS-*h* photocatalysts significantly quench, indicating that the presence of NiS on the surfaces of CdS can effectively inhibit the recombination of electrons and holes in both cases [56]. However, it is noted from Fig. 5c that the PL quenching efficiency for NiS/CdS-*h* photocatalysts reaches the maximum as the NiS loading amount is higher than 2%, which suggests that the physically loaded NiS cocatalyst particles tend to form large agglomerates at higher loading amounts due to the weak interaction between NiS and CdS, thereby limiting their capability of extracting photogenerated electrons. In strong contrast, the PL quenching efficiency for NiS/CdS-*e* photocatalysts increases with increasing NiS content, indicating that the in-situ exsolved NiS cocatalyst particles uniformly embed within CdS substrate, which can not only enhance the dispersion of NiS even at higher loading amounts but also promote the interfacial electron transfer to maximize the charge separation efficiency. However, it should be mentioned that the higher PL quenching efficiency obtained at higher NiS contents cannot ensure that the NiS/CdS-*e* photocatalysts can exhibit higher photocatalytic H_2 activity since the aggregation of NiS particles occur at higher contents will reduce the number of accessible active sites, in turn decrease photocatalytic H_2 evolution activity. In addition, to further clarify the charge transfer kinetics, the decay curves of PL emission were measured by time-resolved PL (TRPL) (Fig. 5d and e) to determine the average life time of charge carriers. As shown in Fig. 5f, the average lifetime of charge carriers in NiS/CdS-*h* keeps almost unchanged first and then shortens with increasing NiS loading amount, which can be attributed to the presence of the reverse built-in electric field that not only makes the separation of charges difficult, but also makes the separated charge carriers have a strong tendency to recombine before they can be captured by physically loaded NiS, thus significantly shortening the carrier lifetime especially at higher NiS loadings. Therefore, limited number of photogenerated electrons can be trapped by physically loaded NiS, thus leading to a much lower H_2 evolution activity compared to NiS/CdS-*e*. On the contrary, it is worth of noting that the average lifetime of NiS/CdS-*e* photocatalysts gradually prolongs with the increase of NiS loading amount, suggesting greatly accelerated transfer of charge carriers from CdS substrate to exsolved NiS cocatalyst due to the formation of strongly coupled interface and an built-in electric field at their contact interface, which will sustainably prolong the lifetime of charge carriers to effectively promote the charge separation, as a result, more photogenerated electrons can be captured by exsolved NiS cocatalyst particles and then participate in the $\text{H}^+/\text{H}_2\text{O}$ reduction reaction to form H_2 at a high rate.

Such an effect of the strongly coupled interface in promoting separation and transfer of photogenerated charge carriers was further confirmed by a series of photoelectrochemical and electrochemical measurements. Fig. 6a shows the transient photocurrent response curves of pristine CdS, 2% NiS/CdS-*e*, and 2% NiS/CdS-*h* photoelectrodes under visible light irradiation (300 W Xe lamp, $\geq 420 \text{ nm}$). The pristine CdS photoelectrode shows a low photocurrent density because of the rapid recombination of photogenerated electrons and holes [57]. In contrast to pristine CdS photoelectrode, the 2% NiS/CdS-*h* photoelectrode only exhibits a slightly enhanced photocurrent response, indicating that the

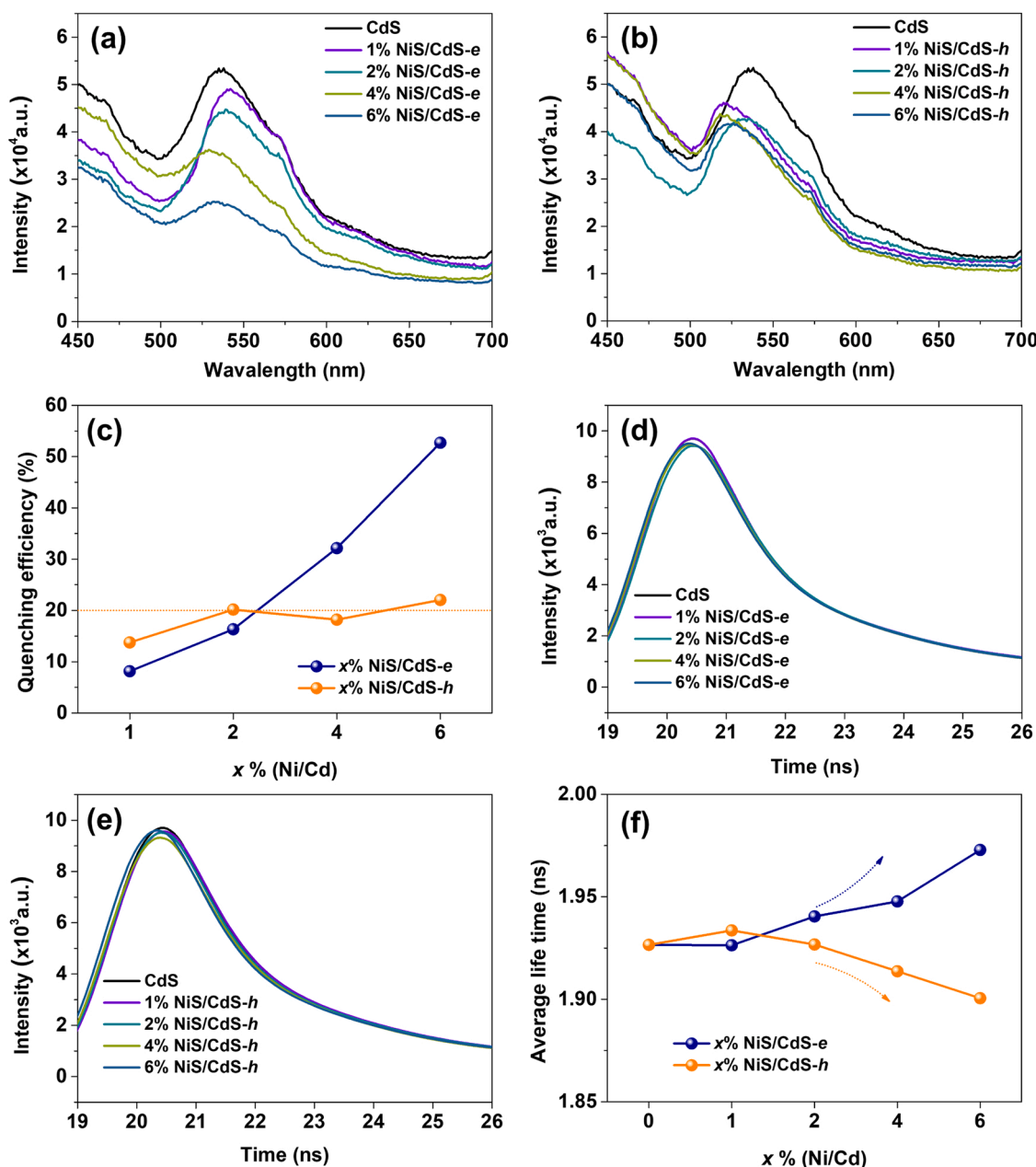


Fig. 5. Steady-state PL emission spectra of (a) x% NiS/CdS-e and (b) x% NiS/CdS-h upon excitation at 370 nm. (c) Quenching efficiency of PL emission for x% NiS/CdS-e and x% NiS/CdS-h. Time-resolved PL emission decay curves of (d) x% NiS/CdS-e and (e) x% NiS/CdS-h. Excitation and detection wavelengths are 370 and 530 nm, respectively. (f) Average PL lifetimes of x% NiS/CdS-e and x% NiS/CdS-h.

physically loaded NiS cocatalyst on CdS is insufficient to promote the charge separation due to the weak interfacial interaction. Notably, the 2% NiS/CdS-e photoelectrode presents a considerably higher photocurrent response than pristine CdS and 2% NiS/CdS-h, clearly demonstrating the rapid electron transfer from excited CdS to exsolved NiS cocatalyst to suppress the charge recombination as a result of the formation of strongly coupled interfaces. The faster electron transfer kinetics of 2% NiS/CdS-e compared to pristine CdS and 2% NiS/CdS-h is also confirmed by electrochemical impedance spectroscopy (EIS) measurements. As shown in the Nyquist plots of Fig. 6b, the arc diameter in the medium frequency region, corresponding to the electron transfer resistance, for 2% NiS/CdS-e is much smaller than that of pristine CdS, and also smaller than that of 2% NiS/CdS-h under both dark and visible light irradiation conditions. This indicates that the large contact area between exsolved NiS cocatalyst and CdS is beneficial for providing low-resistance pathways for fast interfacial electron transfer, which

would facilitate the charge separation and thus enhance the photocatalytic performance [58,59].

Furthermore, electrocatalytic H_2 evolution activity of 2% NiS/CdS-e was tested compared with that of 2% NiS/CdS-h to further highlight the superiority of exsolved 2% NiS cocatalyst. As revealed in Fig. 6c, pristine CdS shows the lowest HER current density due to the lack of active sites [60], while both the 2% NiS/CdS-e and 2% NiS/CdS-h electrodes exhibit enhanced HER current density with applied potential due to the presence of NiS as the H_2 evolution cocatalyst [61]. To further clarify the cocatalytic effect of NiS played in the photocatalytic H_2 evolution reaction, we also prepared pristine NiS and tested its electrocatalytic H_2 evolution activity by linear sweep voltammetry (LSV) measurements under the reaction conditions of photocatalytic H_2 evolution. As shown in Fig. S14, NiS is indeed a highly active catalyst toward H_2 evolution with lower potentials to achieve high current density. In addition, density functional theory (DFT) calculations were performed to study

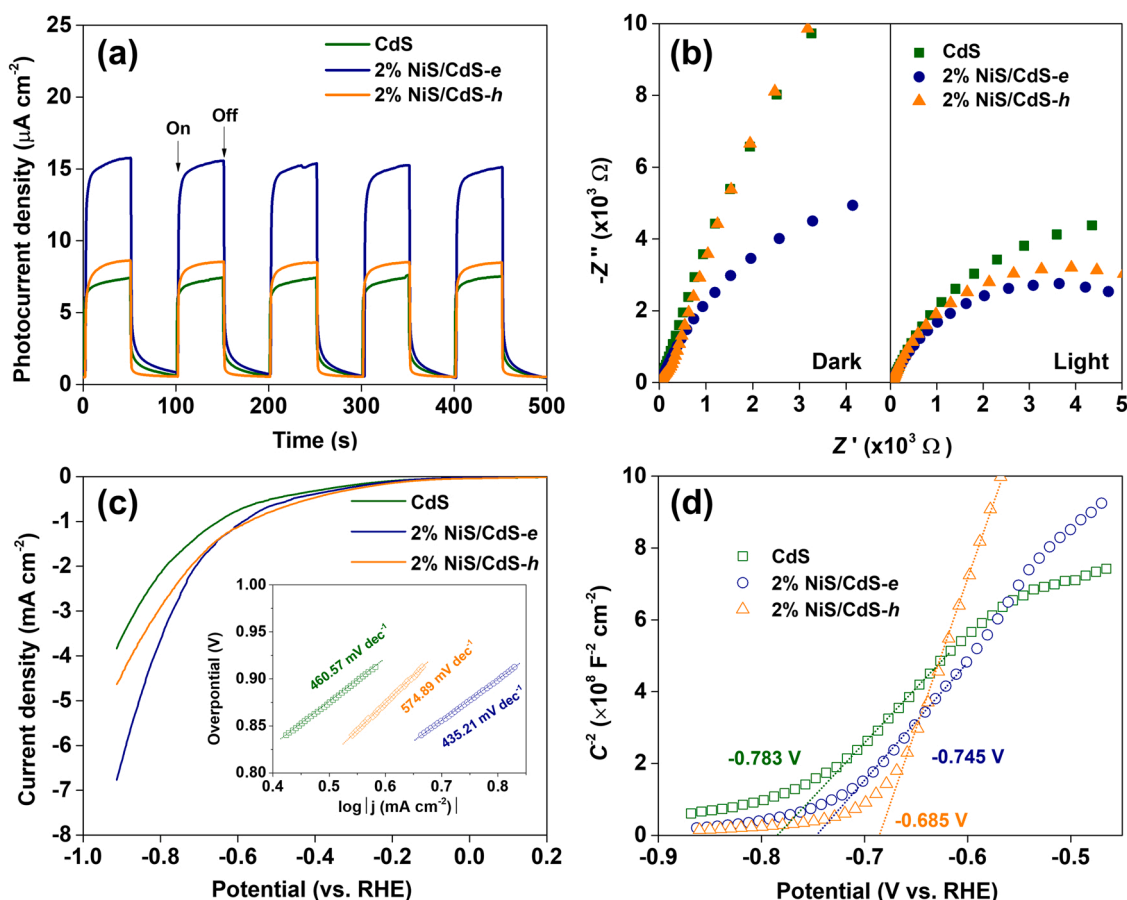


Fig. 6. (a) Transient photocurrent density-time curves, (b) EIS Nyquist plots, (c) Electrocatalytic HER polarization curves, and (d) Mott-Schottky plots of CdS, 2% NiS/CdS-e, and 2% NiS/CdS-h.

the energetics of H adsorption on different sites (Ni and S sites) aiming to identify the main active sites for H_2 evolution reaction over NiS cocatalyst. The calculation results show that both the Ni and S sites have moderate Gibbs free energy (ΔG_{H}) for the atomic hydrogen adsorption and the formation of S-H bond is more thermodynamically favorable than the formation of Ni-H bond, suggesting that the S sites on NiS cocatalyst are the main active sites for the H_2 evolution reaction. However, it can be observed that the 2% NiS/CdS-e exhibits a much higher current density for H_2 evolution and smaller Tafel slope than 2% NiS/CdS-h. This result clearly demonstrates that the exsolved NiS cocatalyst is more active than physically loaded NiS in catalyzing H_2

evolution reactions owing to the enhanced dispersion and strong interfacial interaction [62].

Additionally, the effect of exsolved and physically loaded NiS cocatalyst on the band structures of resulting photocatalysts were also studied by Mott-Schottky analysis. The flat band potential (E_{fb}) for pristine CdS is determined to be -0.783 V vs. RHE, which lowers to -0.745 and -0.685 V vs. RHE for 2% NiS/CdS-e and 2% NiS/CdS-h, respectively. In combination with the band gaps determined from UV-DRS analysis, the valence band (VB) potentials for pristine CdS, 2% NiS/CdS-e, and 2% NiS/CdS-h are determined to be 1.50, 1.53, and 1.59 V vs. RHE, respectively. These results indicate that the physical

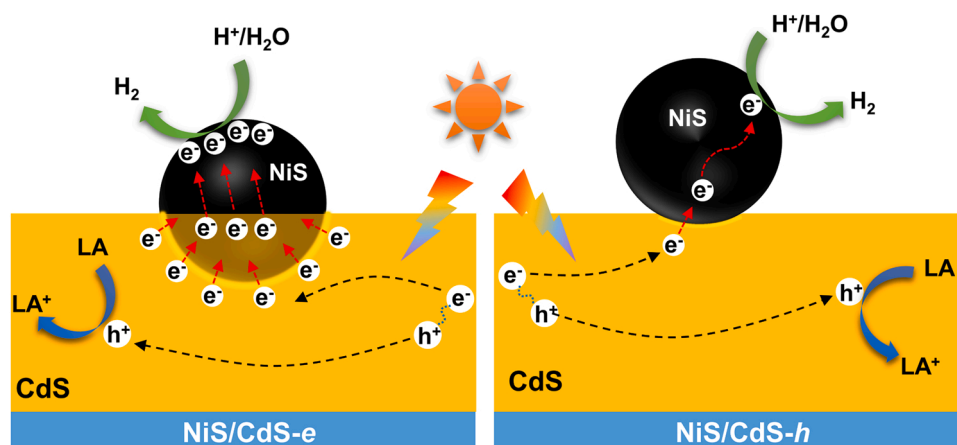


Fig. 7. Photocatalytic H_2 evolution mechanisms over NiS/CdS-e and NiS/CdS-h under visible light irradiation.

loading of NiS cocatalyst on CdS would largely reduce the reductive potential of photogenerated electrons, but the in-situ exsolved NiS cocatalyst could keep the reductive ability of photogenerated electrons while provide highly active sites for enhancing the photocatalytic H₂ activity.

Based on the above experimental results, a photocatalytic mechanism is proposed to explain the enhanced photocatalytic H₂ activity of NiS/CdS-*e* photocatalyst. As shown in Fig. 7, since the exsolved NiS cocatalyst particles are socketed within CdS substrate, a larger contact area between exsolved NiS particles and CdS will be created at the interface compared to limited contact area in NiS/CdS-*h*. As a result, more photogenerated electrons can readily transfer from the excited CdS to exsolved NiS particles with low resistance in NiS/CdS-*e* photocatalyst, thus achieving an enhanced efficient charge separation efficiency and thus ensuring more photogenerated electrons participating in the subsequent H₂ evolution reaction. In addition, the exsolved NiS cocatalyst possess a much higher dispersion and smaller size than physically loaded one, which would also beneficial for providing more active sites with high activity for H₂ evolution.

4. Conclusions

In summary, we have rationally designed and fabricated a strongly coupled NiS-socketed CdS photocatalyst (NiS/CdS-*e*) via a simple in-situ exsolution method for highly efficient photocatalytic H₂ evolution under visible light irradiation. The as-prepared NiS/CdS-*e* features a large contact area between exsolved NiS cocatalyst and CdS substrate, leading to fast electron transfer and thereby enhanced charge separation. In addition, the exsolved NiS cocatalyst particles feature high dispersion and thus exhibits high activity toward H₂ evolution reaction. Benefitting from the above structural merits and compositional features, the NiS/CdS-*e* presents an exceptionally high H₂ evolution rate of 18.9 mmol g⁻¹ h⁻¹ and an apparent quantum efficiency of 13.9% at 420 nm, which much superior to pristine CdS and even much higher than that of NiS/CdS-*h* prepared by impregnation-hydrothermal sulfurization. More importantly, the strongly coupled interface enables NiS/CdS-*e* an excellent stability over a period of 30 h continuous reaction. The in-situ exsolution strategy developed in this work provides a new avenue for the development of strongly coupled cocatalyst/semiconductor photocatalysts for high-performance and durable solar energy conversion.

CRedit authorship contribution statement

Kailu Li: Conceptualization, Methodology, Investigation, Writing – original draft. **Hui Pan:** Formal analysis. **Fang Wang:** Investigation, Formal analysis. **Zhengguo Zhang:** Investigation. **Shixiong Min:** Supervision, Writing – review & editing.

Declaration of Competing Interest

The authors declare that they have no known competing financial interests or personal relationships that could have appeared to influence the work reported in this paper.

Data availability

Data will be made available on request.

Acknowledgements

This work was supported by the National Natural Science Foundation of China (22162001), the Natural Science Foundation of Ningxia Province (2022AAC02040), the Leading Talents Program of Science and Technology Innovation in Ningxia Province (2020GKLRX14), the West Light Foundation of the Chinese Academy of Sciences (XAB2020YW11), the Foundation of Academic Top-notch Talent Support Program of the

North Minzu University (2019BGBZ08), and the Innovation and Entrepreneurship Projects for Returnees of Ningxia Province.

Appendix A. Supporting information

Supplementary data associated with this article can be found in the online version at doi:10.1016/j.apcatb.2022.122028.

References

- [1] T. Takata, J. Jiang, Y. Sakata, M. Nakabayashi, N. Shibata, V. Nandal, K. Seki, T. Hisatomi, K. Domen, Photocatalytic water splitting with a quantum efficiency of almost unity, *Nature* 581 (2020) 411–414, <https://doi.org/10.1038/s41586-020-2278-9>.
- [2] X. Chen, S. Shen, L. Guo, S.S. Mao, Semiconductor-based photocatalytic hydrogen generation, *Chem. Rev.* 110 (2010) 6503–6570, <https://doi.org/10.1021/cr1001645>.
- [3] P. Kuang, M. Sayed, J. Fan, B. Cheng, J. Yu, 3D graphene-based H₂-production photocatalyst and electrocatalyst, *Adv. Energy Mater.* 10 (2020) 1903802, <https://doi.org/10.1002/aenm.201903802>.
- [4] H. Nishiyama, T. Yamada, M. Nakabayashi, Y. Maehara, M. Yamaguchi, Y. Kuromiya, H. Tokudome, S. Akiyama, T. Watanabe, R. Narushima, S. Okunaka, N. Shibata, T. Takata, T. Hisatomi, K. Domen, Photocatalytic solar hydrogen production from water on a 100 m²-scale, *Nature* 598 (2021) 304–307, <https://doi.org/10.1038/s41586-021-03907-3>.
- [5] L. Cheng, Q. Xiang, Y. Liao, H. Zhang, CdS-based photocatalysts, *Energy Environ. Sci.* 11 (2018) 1362–1391, <https://doi.org/10.1039/C7EE03640J>.
- [6] B. Weng, M.Y. Qi, C. Han, Z.R. Tang, Y.J. Xu, Photocorrosion inhibition of semiconductor-based photocatalysts: basic principle, current development, and future perspective, *ACS Catal.* 9 (2019) 4642–4687, <https://doi.org/10.1021/acscatal.9b00313>.
- [7] P. Zhang, X.W. Lou, Design of heterostructured hollow photocatalysts for solar-to-chemical energy conversion, *Adv. Mater.* 31 (2019), e1900281, <https://doi.org/10.1002/adma.201900281>.
- [8] H.G. Yu, F.Y. Chen, F. Chen, X.F. Wang, In-situ self-transformation synthesis of g-C₃N₄-modified CdS heterostructure with enhanced photocatalytic activity, *Appl. Surf. Sci.* 358 (2015) 385–392, <https://doi.org/10.1016/j.apsusc.2015.06.074>.
- [9] Q.Z. Huang, Y. Xiong, Q. Zhang, H.C. Yao, Z.J. Li, Noble metal-free MoS₂ modified Mn_{0.25}Cd_{0.75}S for highly efficient visible-light driven photocatalytic H₂ evolution, *Appl. Catal. B: Environ.* 209 (2017) 514–522, <https://doi.org/10.1016/j.apcatb.2017.03.035>.
- [10] L. Tian, S.X. Min, F. Wang, Integrating noble-metal-free metallic vanadium carbide cocatalyst with CdS for efficient visible-light-driven photocatalytic H₂ evolution, *Appl. Catal. B: Environ.* 259 (2019), 118029, <https://doi.org/10.1016/j.apcatb.2019.118029>.
- [11] L. Tian, S.X. Min, Y.G. Lei, S. Chen, F. Wang, Vanadium carbide: an efficient, robust, and versatile cocatalyst for photocatalytic hydrogen evolution under visible light, *Chem. Commun.* 55 (2019) 6870–6873, <https://doi.org/10.1039/C9CC03230D>.
- [12] Y. Xue, S.X. Min, J. Meng, X. Liu, Y.G. Lei, L. Tian, F. Wang, Light-induced confined growth of amorphous Co doped MoS₂ nanodots on TiO₂ nanoparticles for efficient and stable in-situ photocatalytic H₂ evolution, *Int. J. Hydrog. Energ.* 44 (2019) 8133–8143, <https://doi.org/10.1016/j.ijhydene.2019.02.057>.
- [13] P.W. Du, R. Eisenberg, Catalysts made of earth-abundant elements (Co, Ni, Fe) for water splitting: recent progress and future challenges, *Energy Environ. Sci.* 5 (2012) 6012–6021, <https://doi.org/10.1039/C2EE03250C>.
- [14] Z.W. Mei, B.K. Zhang, J.X. Zheng, S. Yuan, Z.Q. Zhuo, X.G. Meng, Z.H. Chen, K. Amine, W.L. Yang, L. Wang, W. Wang, S.F. Wang, Q. Gong, J. Li, F. Liu, F. Pan, Tuning Cu dopant of Zn_{0.5}Cd_{0.5}S nanocrystals enables high-performance photocatalytic H₂ evolution from water splitting under visible-light irradiation, *Nano Energy* 26 (2016) 405–416, <https://doi.org/10.1016/j.nanoen.2016.05.051>.
- [15] B.J. Ma, S.P. Zhang, W. Wang, L. Feng, R.S. Zhang, K.Y. Lin, D.K. Li, H.J. Zhan, X. Yang, A Novel earth-abundant W-WC heterojunction as efficient co-catalyst for enhanced photocatalytic H₂ evolution, *ChemCatChem* 12 (2020) 1148–1155, <https://doi.org/10.1002/cctc.201901950>.
- [16] Y.L. Li, Q. Zhao, S.J. Liu, G. Ma, Y. Liu, R.H. Liu, H.Y. Mu, X.H. Li, F.T. Li, Tuning electronic structure via CoS clusters for visual photocatalytic H₂ production and mechanism insight, *Chem. Eng. J.* 446 (2022), 137399, <https://doi.org/10.1016/j.cej.2022.137399>.
- [17] L.J. Shen, M.B. Luo, Y.H. Liu, R.W. Liang, F.F. Jing, L. Wu, Noble-metal-free MoS₂ co-catalyst decorated UiO-66/CdS hybrids for efficient photocatalytic H₂ production, *Appl. Catal. B: Environ.* 166–167 (2015) 445–453, <https://doi.org/10.1016/j.apcatb.2014.11.056>.
- [18] B. Han, S. Liu, N. Zhang, Y.J. Xu, Z.R. Tang, One-dimensional CdS@MoS₂ core-shell nanowires for boosted photocatalytic hydrogen evolution under visible light, *Appl. Catal. B: Environ.* (2021) 298–304, <https://doi.org/10.1016/j.apcatb.2016.09.023>.
- [19] W. Zhang, Y.B. Wang, Z. Wang, Z.Y. Zhong, R. Xu, Highly efficient and noble metal-free NiS/CdS photocatalysts for H₂ evolution from lactic acid sacrificial solution under visible light, *Chem. Commun.* 46 (2010) 7631–7633, <https://doi.org/10.1039/C0CC01562H>.
- [20] F. Zhang, H.Q. Zhuang, W.M. Zhang, J. Yin, F.H. Cao, Y.X. Pan, Noble-metal-free CuS/CdS photocatalyst for efficient visible-light-driven photocatalytic H₂

- production from water, *Catal. Today* 330 (2019) 203–208, <https://doi.org/10.1016/j.cattod.2018.03.060>.
- [21] F. Zhang, H.Q. Zhuang, J. Song, Y.L. Men, Y.X. Pan, S.H. Yu, Coupling cobalt sulfide nanosheets with cadmium sulfide nanoparticles for highly efficient visible-light-driven photocatalysis, *Appl. Catal. B: Environ.* 226 (2018) 103–110, <https://doi.org/10.1016/j.apcatb.2017.12.046>.
 - [22] S. Li, Q.Q. Wang, X.L. Yan, H.Q. Zhuang, C. Yuan, J.P. Feng, M.J. Wang, R.F. Li, W. Y. Li, Y.X. Pan, Al_2O_3 support triggering highly efficient photoreduction of CO_2 with H_2O on noble-metal-free $\text{CdS}/\text{Ni}_3\text{S}_2/\text{Al}_2\text{O}_3$, *Appl. Catal. B: Environ.* 240 (2019) 174–181, <https://doi.org/10.1016/j.apcatb.2018.08.060>.
 - [23] L. Zhu, Y. Liu, X.C. Peng, Y.B. Li, Y.L. Men, P. Liu, Y.X. Pan, Noble-metal-free CdS nanoparticle-coated graphene oxide nanosheets favoring electron transfer for efficient photoreduction of CO_2 , *ACS Appl. Mater. Interfaces* 12 (2020) 12892–12900, <https://doi.org/10.1021/acsami.0c00163>.
 - [24] H. Yoshida, R. Yamada, T. Yoshida, Platinum cocatalyst loaded on calcium titanate photocatalyst for water splitting in a flow of water vapor, *ChemSusChem* 12 (2019) 1958–1965, <https://doi.org/10.1002/cssc.201802799>.
 - [25] H. Zhang, L.X. Zhao, F.L. Geng, L.H. Guo, B. Wan, Y. Yang, Carbon dots decorated graphitic carbon nitride as an efficient metal-free photocatalyst for phenol degradation, *Appl. Catal. B: Environ.* (180) (2016) 656–662, <https://doi.org/10.1002/apcatb.2015.06.056>.
 - [26] G.W. Busser, B. Mei, A. Pougin, J. Strunk, R. Gutkowski, W. Schuhmann, M. G. Willinger, R. Schlögl, M. Muhler, Photodeposition of copper and chromia on gallium oxide: the role of co-catalysts in photocatalytic water splitting, *ChemSusChem* 7 (2014) 1030–1034, <https://doi.org/10.1002/cssc.201301065>.
 - [27] N. Qin, J.H. Xiong, R.W. Liang, Y.H. Liu, S. Zhang, Y.H. Li, Z.H. Li, L. Wu, Highly efficient photocatalytic H_2 evolution over $\text{MoS}_2/\text{CdS}-\text{TiO}_2$ nanofibers prepared by an electrospraying mediated photodeposition method, *Appl. Catal. B: Environ.* 202 (2017) 374–380, <https://doi.org/10.1016/j.apcatb.2016.09.040>.
 - [28] Y.C. Zhang, L. Yao, G.S. Zhang, D.D. Dionysiou, J. Li, X.H. Du, One-step hydrothermal synthesis of high-performance visible-light-driven $\text{SnS}_2/\text{SnO}_2$ nanoheterojunction photocatalyst for the reduction of aqueous Cr(VI) , *Appl. Catal. B: Environ.* 144 (2014) 730–738, <https://doi.org/10.1016/j.apcatb.2013.08.006>.
 - [29] A.P. Wu, C.G. Tian, Y.Q. Jiao, Q. Yan, G.Y. Yang, H.G. Fu, Sequential two-step hydrothermal growth of MoS_2/CdS core-shell heterojunctions for efficient visible light-driven photocatalytic H_2 evolution, *Appl. Catal. B: Environ.* 203 (2017) 955–963, <https://doi.org/10.1016/j.apcatb.2016.11.009>.
 - [30] D.T. Nguyen, C.C. Nguyen, M. St-Jean, S. Chabot, S. Kaliaguine, T.O. Do, All in one: contributions of Ni dopants and Ni/NiS dual cocatalysts to the enhanced efficiency of TiO_2 photocatalyst for the degradation of organic pollutants, *ACS Appl. Nano Mater.* 1 (2018) 6864–6873, <https://doi.org/10.1021/acsanm.8b01693>.
 - [31] D. Neagu, G. Tsekouras, D.N. Miller, H. Menard, J.T. Irvine, In-situ growth of nanoparticles through control of non-stoichiometry, *Nat. Chem.* 5 (2013) 916–923, <https://doi.org/10.1038/nchem.1773>.
 - [32] Y.F. Sun, Y.Q. Zhang, J. Chen, J.H. Li, Y.T. Zhu, Y.M. Zeng, B.S. Amirkhiz, J. Li, B. Hua, J.L. Luo, New opportunity for in-situ exsolution of metallic nanoparticles on perovskite parent, *Nano Lett.* (16) (2016) 5303–5309, <https://doi.org/10.1021/acs.nanolett.6b02757>.
 - [33] K.K. Hansen, K.V. Hansen, A-site deficient $(\text{La}_{0.6}\text{Sr}_{0.4})_{1-x}\text{Fe}_{0.8}\text{Co}_{0.2}\text{O}_{3-\delta}$ perovskites as SOFC cathodes, *Solid State Ion.* 178 (2007) 1379–1384, <https://doi.org/10.1016/j.ssi.2007.07.012>.
 - [34] B.S. Kang, J. Matsuda, T. Ishihara, Cu–Fe–Ni nano alloy particles obtained by exsolution from $\text{Cu(Ni)Fe}_2\text{O}_4$ as active anode for SOFCs, *J. Mater. Chem. A* 7 (2019) 26105–26115, <https://doi.org/10.1039/C9TA09482B>.
 - [35] K.P. Jiang, Z.K. Liu, G.R. Zhang, W.Q. Jin, A novel catalytic membrane reactor with homologous exsolution-based perovskite catalyst, *J. Membr. Sci.* 608 (2020), 118213, <https://doi.org/10.1016/j.memsci.2020.118213>.
 - [36] L.M. Yang, K. Xie, S.S. Xu, T.S. Wu, Q. Zhou, T. Xie, Y.C. Wu, Redox-reversible niobium-doped strontium titanate decorated with in-situ grown nickel nanocatalyst for high-temperature direct steam electrolysis, *Dalton Trans.* 43 (2014) 14147–14157, <https://doi.org/10.1039/C4DT01430H>.
 - [37] L.C. Seitz, C.F. Dickens, K. Nishio, Y. Hikita, J. Montoya, A. Doyle, C. Kirk, A. Vojvodic, H.Y. Hwang, J.K. Nørskov, T.F. Jaramillo, A highly active and stable $\text{IrO}_x/\text{SrIrO}_3$ catalyst for the oxygen evolution reaction, *Science* 353 (2016) 1011–1014, <https://doi.org/10.1126/science.aaf5050>.
 - [38] E. Cho, Y.H. Lee, H. Kim, E.J. Jang, J.H. Kwak, K. Lee, C.H. Ko, W.L. Yoon, Ni catalysts for dry methane reforming prepared by A-site exsolution on mesoporous defect spinel magnesium aluminate, *Appl. Catal. A-Gen.* 602 (2020), 117694, <https://doi.org/10.1016/j.apcata.2020.117694>.
 - [39] E. le Saché, L. Pastor-Pérez, D. Watson, A. Sepúlveda-Escribano, T.R. Reina, Ni stabilised on inorganic complex structures: superior catalysts for chemical CO_2 recycling via dry reforming of methane, *Appl. Catal. B: Environ.* 236 (2018) 458–465, <https://doi.org/10.1016/j.apcatb.2018.05.051>.
 - [40] Y.F. Sun, Y.L. Yang, J. Chen, M. Li, Y.Q. Zhang, J.H. Li, B. Hua, J.L. Luo, Toward a rational photocatalyst design: a new formation strategy of co-catalyst/semiconductor heterostructures via in-situ exsolution, *Chem. Commun.* 54 (2018) 1505–1508, <https://doi.org/10.1039/C7CC08797G>.
 - [41] J.X. Yu, L. Zhang, J. Qian, Z.R. Zhu, S. Ni, G. Liu, X.X. Xu, In-situ exsolution of silver nanoparticles on $\text{AgTaO}_3\text{-SrTiO}_3$ solid solutions as efficient plasmonic photocatalysts for water splitting, *Appl. Catal. B: Environ.* 256 (2019), 117818, <https://doi.org/10.1016/j.apcatb.2019.117818>.
 - [42] J. Li, Y.H. Ni, J. Liu, J.M. Hong, Preparation, conversion, and comparison of the photocatalytic property of Cd(OH)_2 , CdO , CdS and CdSe , *J. Phys. Chem. Solids* 70 (2009) 1285–1289, <https://doi.org/10.1016/j.jpcs.2009.07.014>.
 - [43] A. Rmili, F. Ouachtari, A. Bouaoud, A. Louardi, T. Chtouki, B. Elidrissi, H. Erguig, Structural, optical and electrical properties of Ni-doped CdS thin films prepared by spray pyrolysis, *J. Alloy. Compd.* 557 (2013) 53–59, <https://doi.org/10.1016/j.jallcom.2012.12.136>.
 - [44] L. Tian, S.X. Min, F. Wang, Z.G. Zhang, Metallic vanadium nitride as a noble-metal-free cocatalyst efficiently catalyzes photocatalytic hydrogen production with CdS nanocrystals under visible light irradiation, *J. Phys. Chem. C* 123 (2019) 28640–28650, <https://doi.org/10.1021/acs.jpcc.9b09389>.
 - [45] C.H. Li, H.M. Wang, S.B. Naghadeh, J.Z. Zhang, P.F. Fang, Visible light driven hydrogen evolution by photocatalytic reforming of lignin and lactic acid using one-dimensional NiS/CdS nanostructures, *Appl. Catal. B: Environ.* 227 (2018) 229–239, <https://doi.org/10.1016/j.apcatb.2018.01.038>.
 - [46] R.C. Gao, L.Y. Xiong, L. Huang, W. Chen, X.Y. Li, X.Q. Liu, L.Q. Mao, A new structure of $\text{Pt NF@Ni(OH)}_2/\text{CdS}$ heterojunction: preparation, characterization and properties in photocatalytic hydrogen generation, *Chem. Eng. J.* 430 (2022), 132726, <https://doi.org/10.1016/j.cej.2021.132726>.
 - [47] Y. Yang, A.Q. Meng, X.L. Jiang, S.G. Meng, X.Z. Zheng, S.J. Zhang, X.L. Fu, S. F. Chen, Photocatalytic performance of NiS/CdS composite with multistage structure, *ACS Appl. Energy Mater.* 3 (2020) 7736–7745, <https://doi.org/10.1021/acsaem.0c01133>.
 - [48] S.D. Guan, X.L. Fu, Y. Zhang, Z.J. Peng, beta-NiS modified CdS nanowires for photocatalytic H_2 evolution with exceptionally high efficiency, *Chem. Sci.* 9 (2018) 1574–1585, <https://doi.org/10.1039/C7SC03928J>.
 - [49] K. Chang, Z.W. Mei, T. Wang, Q. Kang, S.X. Ouyang, J.H. Ye, $\text{MoS}_2/\text{graphene}$ cocatalyst for efficient photocatalytic H_2 evolution under visible light irradiation, *ACS Nano* 8 (2014) 7078–7087, <https://doi.org/10.1021/nn5019945>.
 - [50] R.B. Wei, Z.L. Huang, G.H. Gu, Z. Wang, L.X. Zeng, Y.B. Chen, Z.Q. Liu, Dual-cocatalysts decorated rimous CdS spheres advancing highly-efficient visible-light photocatalytic hydrogen production, *Appl. Catal. B: Environ.* 231 (2018) 101–107, <https://doi.org/10.1016/j.apcatb.2018.03.014>.
 - [51] Y. Xia, B. Cheng, J.J. Fan, J.G. Yu, G. Liu, Unraveling photoexcited charge transfer pathway and process of $\text{CdS}/\text{Graphene}$ nanoribbon composites toward visible-light photocatalytic hydrogen evolution, *Small* 15 (2019) 1902459, <https://doi.org/10.1002/sml.201902459>.
 - [52] B.W. He, C.B. Bie, X.G. Fei, B. Cheng, J.G. Yu, W.K. Ho, A. Al-Ghamdi, S. Wageh, Enhancement in the photocatalytic H_2 production activity of CdS NRs by Ag_2S and NiS dual cocatalysts, *Appl. Catal. B: Environ.* 288 (2021) 0926–3373, <https://doi.org/10.1016/j.apcatb.2021.119994>.
 - [53] X.W. Shi, S.Y. Kim, M. Fujitsuka, T. Majima, In-situ observation of NiS nanoparticles depositing on single TiO_2 mesocrystal for enhanced photocatalytic hydrogen evolution activity, *Appl. Catal. B: Environ.* 254 (2019) 594–600, <https://doi.org/10.1016/j.apcatb.2019.05.031>.
 - [54] Y.G. Lei, C. Yang, J.H. Hou, F. Wang, S.X. Min, X. Ma, Z. Jin, J. Xu, G. Lu, K. Huang, Strongly coupled $\text{CdS}/\text{graphene}$ quantum dots nanohybrids for highly efficient photocatalytic hydrogen evolution: unraveling the essential roles of graphene quantum dots, *Appl. Catal. B: Environ.* 216 (2017) 59–69, <https://doi.org/10.1016/j.apcatb.2017.05.063>.
 - [55] L. Shang, B. Tong, H.J. Yu, G. Waterhouse, C. Zhou, Y.F. Zhao, M. Tahir, L. Wu, C. H. Tung, T.R. Zhang, CdS nanoparticle-decorated Cd nanosheets for efficient visible light-driven photocatalytic hydrogen evolution, *Adv. Energy Mater.* 6 (2016) 1501241–1501248, <https://doi.org/10.1002/aenm.201501241>.
 - [56] X. Lu, C.Y. Toe, F. Ji, W. Chen, X. Wen, R.J. Wong, J. Seidel, J. N. Hart, Y. H. Ng, Light-induced formation of MoO_3S_y clusters on CdS nanorods as cocatalyst for enhanced hydrogen evolution, *ACS Appl. Mater. Interfaces* 12 (2020) 8324–8332, <https://doi.org/10.1021/acsami.9b21810>.
 - [57] Y.P. Xie, Z.B. Yu, G. Liu, X.L. Ma, H.M. Cheng, CdS -mesoporous ZnS core-shell particles for efficient and stable photocatalytic hydrogen evolution under visible light, *Energy Environ. Sci.* 7 (2014) 1895–1901, <https://doi.org/10.1039/c3ee43750g>.
 - [58] G.S. Li, L. Wu, F. Li, P.P. Xu, D.Q. Zhang, H.X. Li, Photoelectrocatalytic degradation of organic pollutants via a CdS quantum dots enhanced TiO_2 nanotube electrode under visible light irradiation, *Nanoscale* 5 (2013) 2118–2125, <https://doi.org/10.1039/C3NR34253K>.
 - [59] G.G. Liu, G.X. Zhao, W. Zhou, Y.Y. Liu, H. Pang, H.B. Zhang, D. Hao, X.G. Meng, P. Li, T. Kako, J.H. Ye, In-situ bond modulation of graphitic carbon nitride to construct p-n homojunctions for enhanced photocatalytic hydrogen production, *Adv. Funct. Mater.* 26 (2016) 6822–6829, <https://doi.org/10.1002/adfm.201602779>.
 - [60] K.L. He, J. Xie, Z.H. Yang, R.C. Shen, Y.P. Fang, S. Ma, X.B. Chen, X. Li, Earthabundant WC nanoparticles as an active noble-metal-free co-catalyst for the highly boosted photocatalytic H_2 production over $\text{g-C}_3\text{N}_4$ nanosheets under visible light, *Catal. Sci. Technol.* 7 (2017) 1193–1202, <https://doi.org/10.1039/C7CY00029D>.
 - [61] X. Peng, T. Sk. Mahasin Alam, X.M. Larissa, J. Ge, K. Fu, J.Y. Huo, Wang, Molybdenum phosphide as an efficient electrocatalyst for the hydrogen evolution reaction, *Energy Environ. Sci.* 7 (2014) 2624–2629, <https://doi.org/10.1039/C4EE00957F>.
 - [62] X. Peng, L.S. Hu, L. Wang, X.M. Zhang, J.J. Fu, K.F. Huo, L. Lee, K.Y. Wong, P. Chu, Vanadium carbide nanoparticles encapsulated in graphitic carbon network nanosheets: a high efficiency electrocatalyst for hydrogen evolution reaction, *Nano Energy* 26 (2016) 603–609, <https://doi.org/10.1016/j.nanoen.2016.06.020>.